Pattern recognition for COMPASS RICH 1

Progress Report - February '99.

P. Schiavon

Abstract

A pattern recognition method for the identification of *rings* in the RICH 1 in the COMPASS experiment is presented. The method is based on a recipe for the Cerenkov emission angle reconstruction found in the literature. Both resolution and angle reconstruction efficiency are studied with MC events as a function of the event particle multiplicity and other parameters. No particle identification procedure is proposed in this report.

1 Introduction :

The pattern recognition method for the identification of *rings* in the COMPASS RICH 1, which will be discussed, is based on a recipe for the Cerenkov emission angle reconstruction found in the literature (see e.g. : T. Ypsilantis and J. Seguinot, Nucl. Instr. and Methods, A343 (1994) 30) and already described, in the form adapted to the COMPASS software, in the COMPASS Internal Notes by P. Schiavon 'Studies of the Cerenkov emission angle reconstruction Part 1.' (10/6/97) and '... Part 2.' (27/10/97), available on the COMPASS Web page.
The method assumes that the particle trajectory is known at the RICH entrance. It has been used or proposed, with some modifications, for other experiments (Delphi, LHCb).
Angle reconstruction and pattern recognition are strictly related each other and will be discussed together.
Input (simulated) data, essentially the active pads of the photon detector, need to be preliminarly processed by a clustering procedure, which also has been studied and implemented.
The procedure described in this report is not intended to be a particle identification method.

With respect to previous exercises, COMGeant (LEPTO) generated events are used and a full simulation of the behaviour of the photon detector has ben implemented; this has been done mainly by V. Alexakhin (from the RD26 and Alice HMPID code).

2 Geometry of RICH 1 :

Fig.1 is an artistic view of the RICH 1, showing some construction details (photon chambers, mirror arrays, vessel) and in fig.2 a schematic side view of RICH 1 geometry

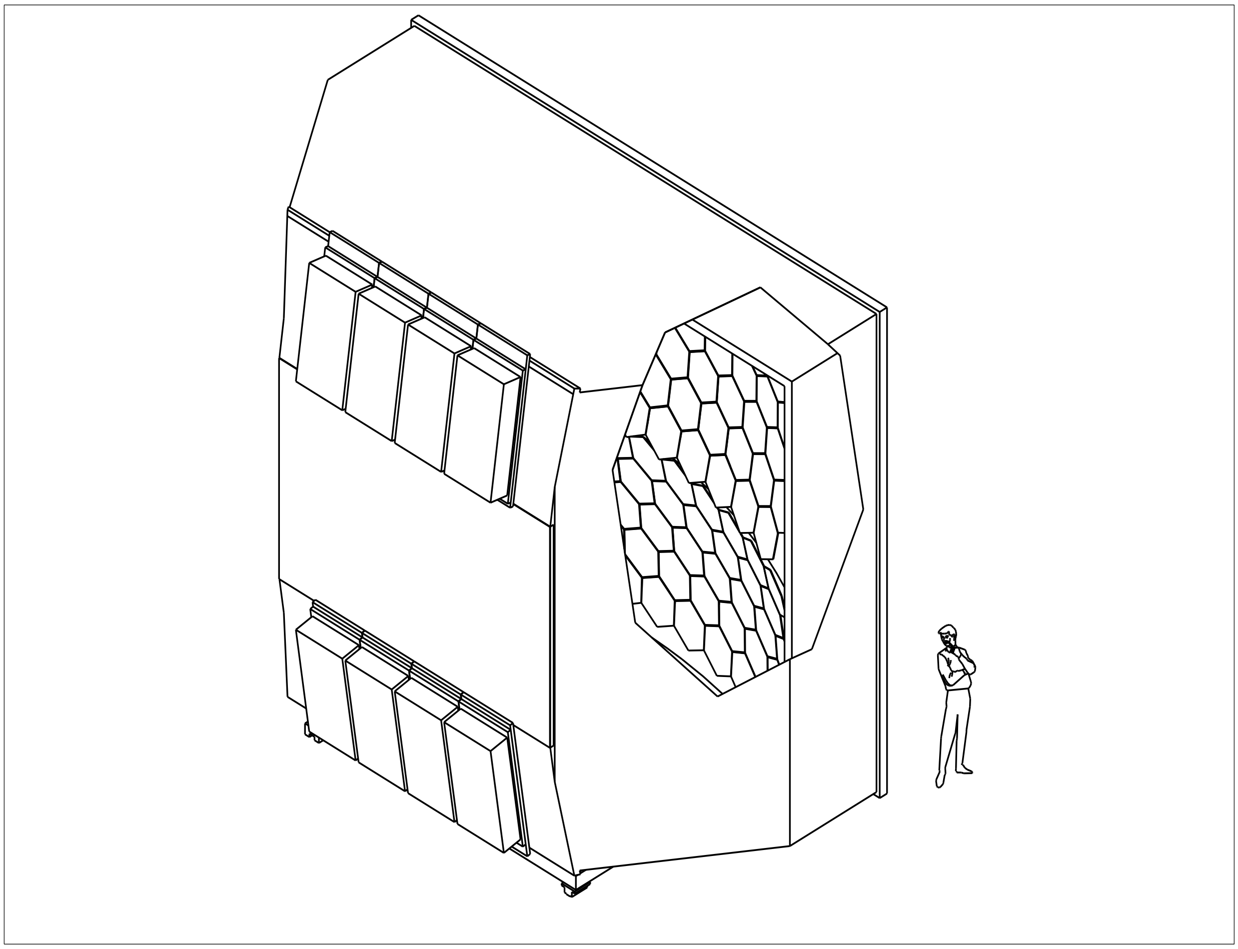

Figure 1: Artistic view of COMPASS RICH 1. Inside the vessel are visible the hexagonal mirror elements which form the upper and the lower reflecting surfaces. On the back of the vessel, the four upper and the four lower photon chambers.

is shown.

• Reference systems.
The following reference systems are defined and used in the reconstruction.

Main Reference System (MRS).

a) The origin of the main reference system is in the nominal centre of the interaction Target (as from COMGeant);
the z-axis is parallel to the beam line, the y-axis vertical and the x-axis horizontal to the left (looking downstream).

Mirror Working Reference (MWR).

b) The origin of the mirror working reference is in the centre of curvature of the upper mirror (MWR_{up}), its z-axis is orthogonal to the upper detector surface and x-axis parallel to the x-axis of MRS; the MWR_{dw} is defined in a similar way.
Each detector surface is tilted by an angle of 150. mrad with respect to the MRS xy-plane,

so that the z-axis of the MWR_{up} makes an angle of -150. mrad with the z-axis of MRS and the MWR_{dw}, +150. mrad.

Detector Reference Systems (DRS).

c) They are defined on the (upper or lower) detector surface, with the origin at the detector centre and x-axis parallel to the x-axis of MRS.

Cathode Reference Systems (CRS).

d) They are defined on the (upper or lower) detector surface, with the origin at the centre of each cathode and axes parallel to those of the DRS's (there are 16 CRS's).

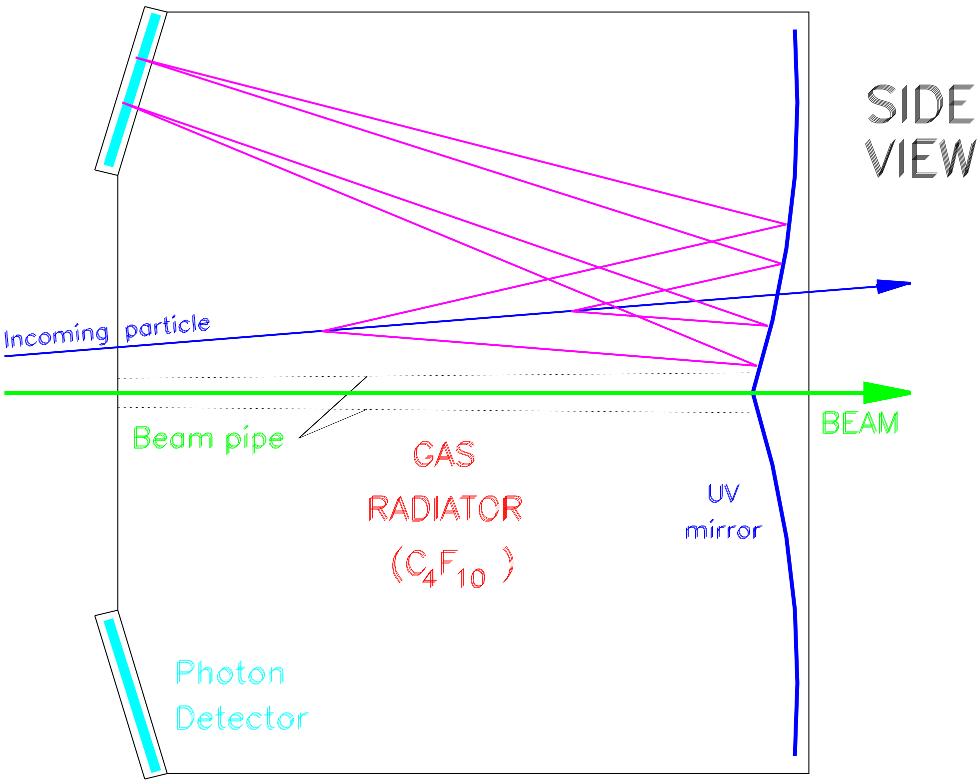

Figure 2: The side schematic view of the RICH shows the relative positions of : the mirrors (blue), the photon detectors (light blue), the beam line (green), the beam pipe (dotted) and some typical photon trajectories (magenta).

- Mirrors.

b) There are two (upper or lower) spherical mirrors with centres in the MRS zy-plane at positions :

upper mirror centre (MRS) : 0. 1600. 1673. mm lower mirror centre (MRS) : 0. - 1600. 1673. mm

In the present description each mirror is a unique spherical surface with equal radii of 6600. mm and no imperfections.
In the reality it will consist of an array of up to sixty hexagonal elements ($\simeq$450.mm diameter), put side by side, (see fig.1) and local imperfections or variations in radius are expected to some extent, as well as dead zones between adjacent elements. Their effects on the RICH resolution have been evaluated separately (see the COMPASS Internal Note by P. Schiavon 'Studies of the effects of mirror radius value ...' (14/5/97), available on the COMPASS Web page, and the RICH98 Conference Proceedings).

• Detectors.

c) The two detectors (upper and lower) have plane surfaces.

Each detector (1-2) consists of four (1-4 and 5-8) photon chambers; each photon chamber of two cathodes (1-8 and 9-16).
Each cathode is made by an array of 72×72 (8.×8.mm^2) pads, for a total of 5184 pads per cathode (576.×576.mm^2) and a grand total of 82944 pads (5.3 m^2 active area).

upper detector centre	(MRS) :	0.	2001.8	5221.8	mm
	(MWR) :	0.	927.7	3449.3.	mm
lower detector centre	(MRS) :	0.	- 2001.8	5221.8	mm
	(MWR) :	0.	- 927.7	3449.3.	mm

cathode centre x and y-positions (DRS) (mm) :

(1, 3, 5, 7)	:	(952.5, 1228.7)	(317.5, 1228.7)	(-317.5, 1228.7)	(-952.5, 1228.7)
(2, 4, 6, 8)	:	(952.5, 626.7)	(317.5, 626.7)	(-317.5, 626.7)	(-952.5, 626.7)
(9, 11, 13, 15)	:	(952.5, -626.7)	(317.5, -626.7)	(-317.5, -626.7)	(-952.5, -626.7)
(10, 12, 14, 16)	:	(952.5,-1228.7)	(317.5,-1228.7)	(-317.5,-1228.7)	(-952.5,-1228.7)

3 Simulation :

To test the procedure, MC generated events are used in the COMGeant framework. Events, simulated by LEPTO generator, are tracked through the COMPASS apparatus (PTarget, solenoid field, trackers, SM 1, trackers, RICH 1) to the RICH exit.
Multiple Coulomb scattering and energy losses are (or are not) taken into account.

For photon generation and propagation, all of the most relevant effects are taken into account (emission density as a function of particle β, losses for absorption in C_4F_{10}, for reflection on mirrors, for detector quartz window crossing, ...) except :
• the photon chromatic dispersion is at present neglected; fixed energy photons ($\simeq$7. eV) are used instead;
• the RICH mirror surfaces are continuous and perfect.
Photons reaching the photocathode surface, through the quartz window, and converting, are written as ntuples on an output file.
Note that, in the present simulation, the average number of converted photons is 20 with respect to the expected number of 34; this figure is obviously affecting both the resolution

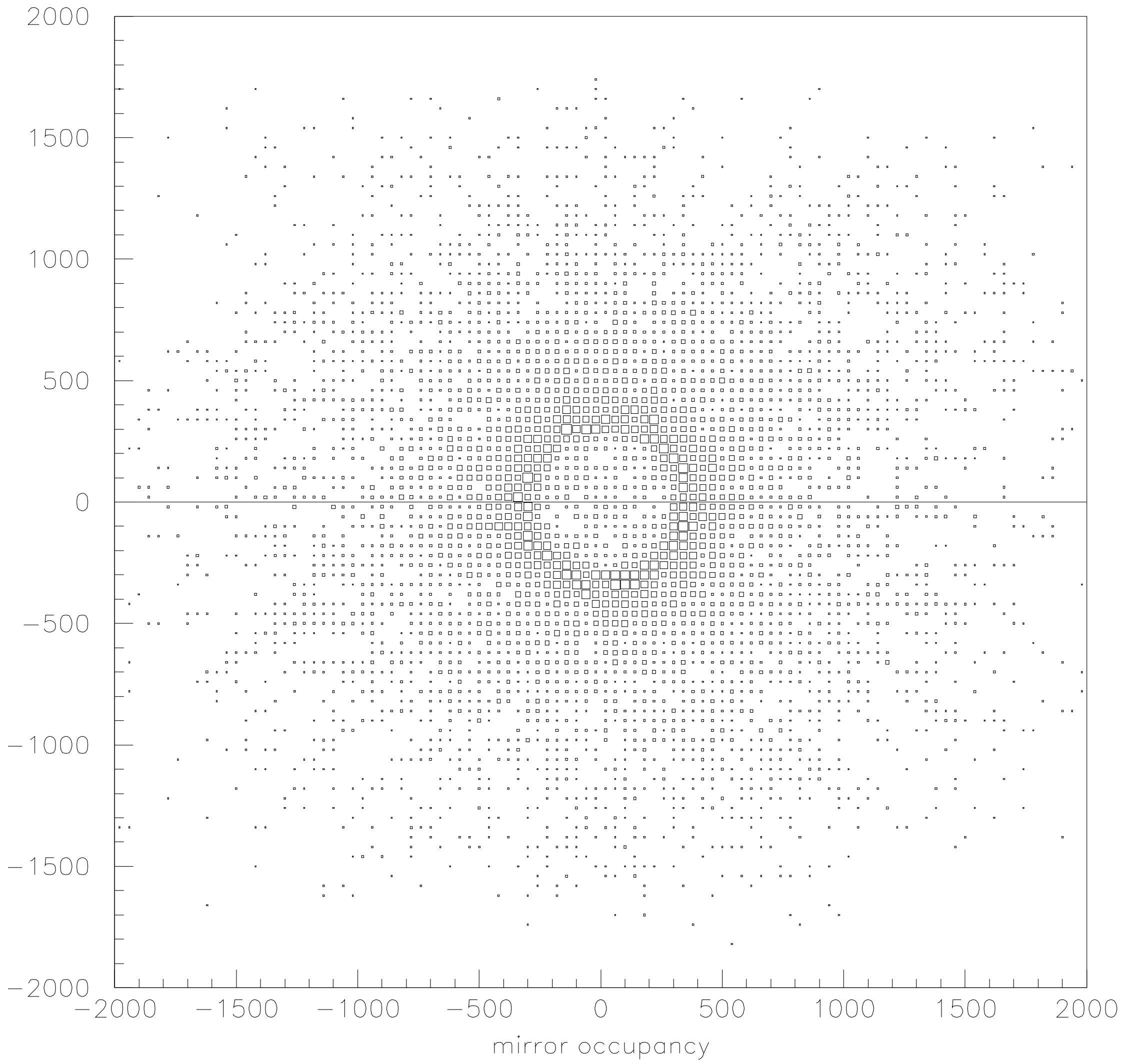

Figure 3: Upper and lower mirror occupancy (LEPTO events). Note the shadow of the beam pipe.

and the efficiency obtained.
These files, corresponding to different conditions, are the input to the second step, in which the detector response is simulated.
The photon chamber structure (cathodes, pads, anode wires, ...) as well as the pulse generation (Pulse Height (PH) distribution, feedback photon generation and conversion, thresholding, pedestal subtraction, electronic noise fraction and distribution, ...) are taken into account.
Note also that a tuning of the procedure as a function of the different operating conditions of the detector (HV's, thresholds, ...) is needed.
The output is the array of the PH of the active pads and their addresses.

For a typical file of LEPTO generated events, the occupancy of the mirrors (fig.3) and of the photon chambers (fig.4) are shown.
In fig.5 the momentum distribution for μ, π and K (a), the β distribution (b) for all the particles and the particle 'impact parameter' (the distance of the particle trajectory to the mirror centre) distribution (c).

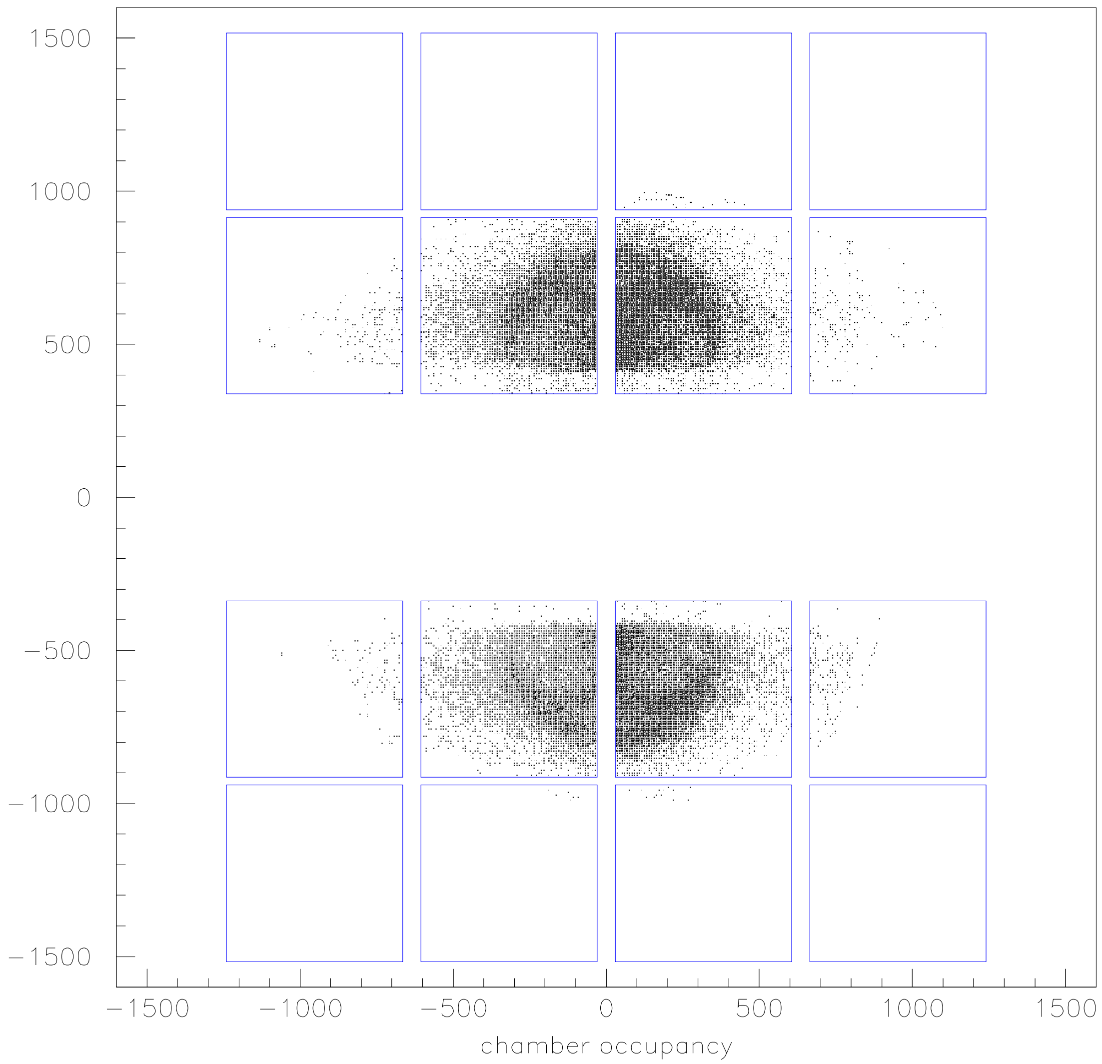

Figure 4: Upper and lower detector occupancy (LEPTO events).

In this simulation, a typical LEPTO event has a particle multiplicity of 2.6 particle/event.
No physical background (beam halo, competitive target scattering, event pileup, ...) is at present simulated; only the electronic noise on the photon detectors is taken into account. The corresponding average number of active pads is $\sim$200.
Note that (compare with fig.4), on the cathodes (4, 6, 11, 13) where the photon density is greater, there are $\simeq 8$ particle/m^2.
To simulate larger particle multiplicities, the single events are summed up in groups ($\times$n) of up to 10; this results in rather 'unphysical' particle distributions which may affect to some (probably limited) extent the validity of the results.
More serious limitations can be expected because of the not simulated beam halo (close and far halo).

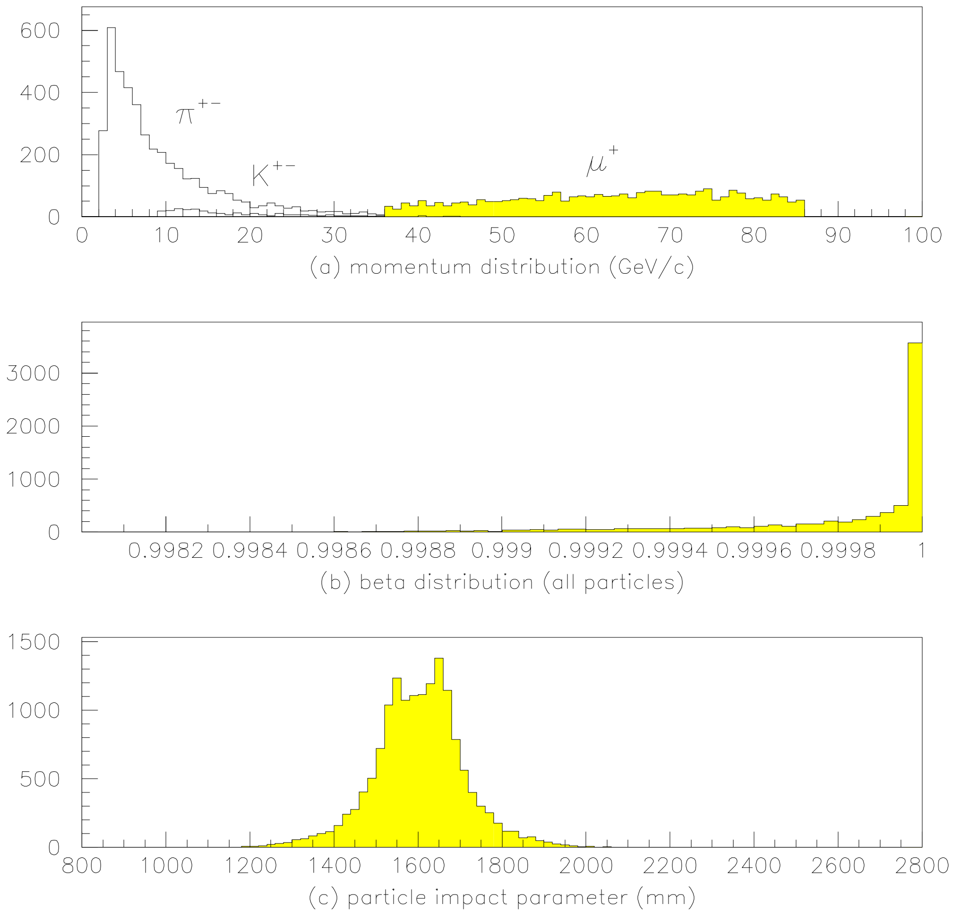

Figure 5: (a) Momentum distribution for μ, π and K in the file; (b) β distribution for all the particles; (c) the particle 'impact parameter' distribution.

4 Procedure :

• Input.
The input to the pattern recognition procedure consists of :

a) from RICH photon chambers,
the PH from the ADC of each pad of the detector which gives a signal and its address, i.e. the cathode number i_c (1-16), the pad number i_x (1-72) along the x-axis and i_y (1-72) along the y-axis (CRS).

b) from the tracking detectors,
for each reconstructed particle, its position at the RICH entrance window, x_p, y_p, z_p, the direction, tg_{xp}, tg_{yp} and the measured momentum p_p.
The particle trajectory is assumed to be measured with good accuracy both in angle and position by external independent detectors.

c) from the MC generation,
the 'true' values (particle masses, photon impacts on the detectors, ...) to be used in the evaluation of the procedures.

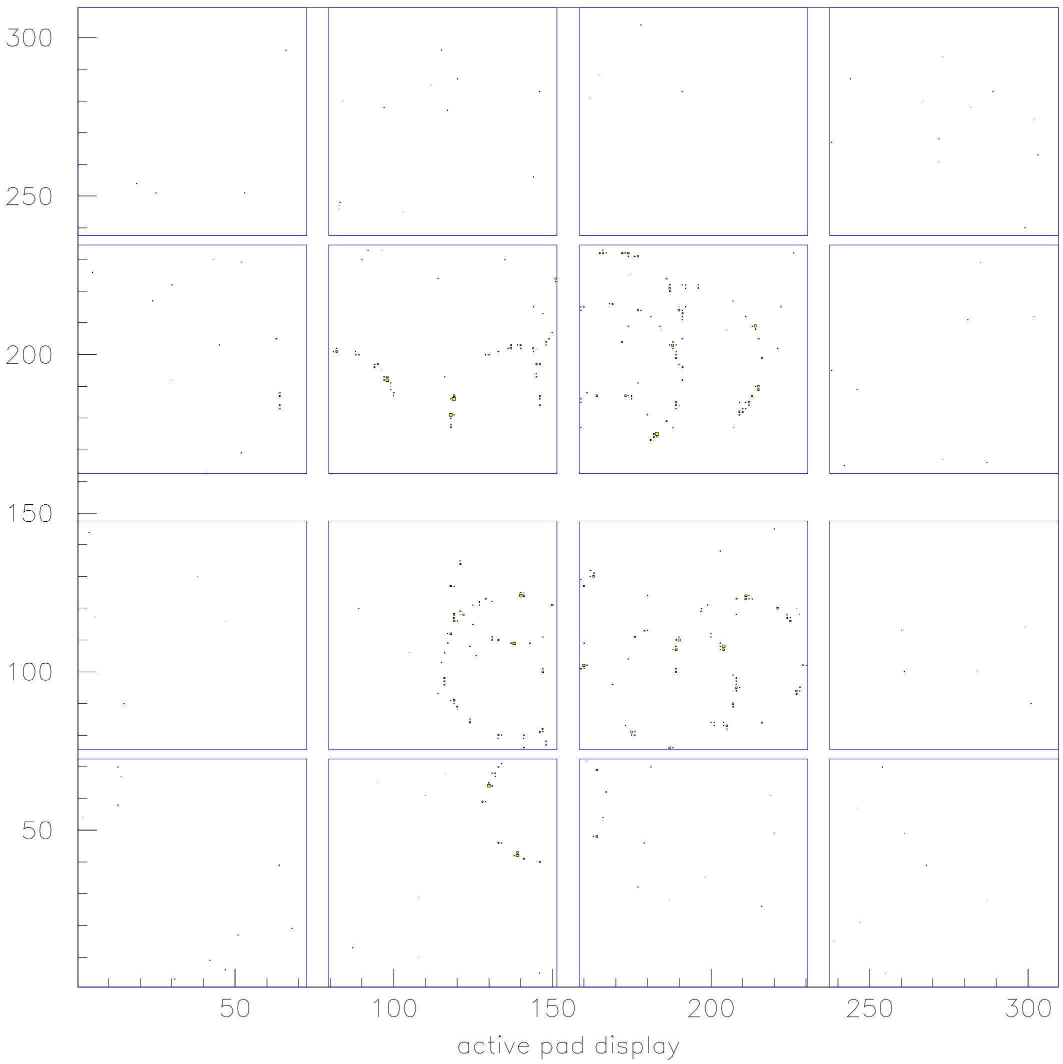

Figure 6: Active pad layout of a 'triple' ($\times 3$) LEPTO event with 12 particles.

• Clustering.

As well known, the active pads are distributed around the photon impact points on the detector surface. To enter the angle riconstruction procedure, the pads may (or may not) be put together in a cluster, which should better correspond to the photon impact point. To set up and optimize the reconstruction line, this procedure was needed, at least as a first approach.

The problem is rather complex and delicate, mainly for high photon densities; the basic procedure is to take some average of the individual pad positions, weighted with the pad PH (centre of mass). This works satisfactorily for isolated clusters, but need some criteria to split contiguous clusters.

To better understand the problem, the simulation of the pulse generation has been used to study the cluster structure, for single photons as well as for many photons in a *ring*.

One of the ingredients to take into account is that the anode wires are along the y (DRS) direction, determining, to some extent, a larger signal induction along y.

In fig.7 some typical distributions of the active pads and their PH's, for direct or feedback photons; in (a) the active pad distribution around the pad hit; in (b) the corresponding PH distribution; in (c) the pad distribution of the first and in (d) of the second PH maxi-

mum around tha pad hit; in (e) the pad distribution when there is one ($\simeq 10\%$) feedback photon converted and in (f) the pad distribution of the PH maximum of the feedback photon.
Average cluster size (3.5), cluster structure and relative frequencies can be evaluated and used in the clustering code.
The clustering procedure works along the following line : the pad of maximum PH is found and adjacent (along x or y only) active pads are put together into the cluster, until their PH are less than 0.3 (along x) or 0.6 (along y) the value of the maximum; otherwise the cluster is split; the cluster addition stops when no more adjacent pads are available and it is restarted for a further cluster looking for the next PH maximum.
In fig.8 there is an exemple of a cathode with some *rings* (or parts) in it: in (a) the layout of the pads as hit by the incoming photons; in (b) the active pads after pulse generation and electronic noise addition; in (c) the cluster distribution; in (d) the clusters belonging to the reconstructed *rings* (see later) together with the 'virtually reflected' particle impact point at the ∼centre of the *ring*; the clustering procedure acts from (b) to (c).

• Angle reconstruction.
Each cluster is assumed to be a photon impact point on the detector plane (DRS).
For each reconstructed particle, we assume that all the photons have been emitted from the middle point of its trajectory inside the radiator (gas) volume (average emission point), computed from the measured particle parameters.
Then for each cluster, the emission polar angles θ_{clu} and ϕ_{clu}, around the particle trajectory, are computed using the procedure mentioned above; in a ϕ_{clu} vs θ_{clu} plot, photons emitted by the selected particle aligne at constant θ_C and distribute uniformly in ϕ_C, whereas photons emitted by the other particles spread along non linear paths; see fig.10 (a) to (c) and (d) to (f).

The knowledge of the incoming particle trajectory allows the evaluation of the 'impact point', on the detector surface, of the particle 'virtually reflected' from the mirror, which is a fairly good approximation of the *ring* centre.
Remember that in our RICH geometry, the *rings* depart appreciably from the circular shape, as a function of the large particle 'impact parameter' (fig.5 (c)).
In principle the situation is further complicated by the fact that the photons emitted by some particles hit both the upper and the lower mirror, being reflected on the two corresponding detectors (see an exemple in fig.11).
An advantage of the angle reconstruction procedure used is that each photon cluster is properly processed independently from the others; both the cited effects are then exactly taken into account.

The *ring* on the detector surface has a 'radius' of up to 182. mm (β=1 particle); the knowledge of the particle 'impact point' on the detector restricts to 4 the number of cathodes (576.×576. mm^2) involved;
this cathode selection reduces the number of useless calculation by an appreciable amount, discarding a lot of clusters which can not be photons emitted by the particle considered.

Moreover, the hits of the photons emitted by each particle cover on the mirror(s) surface a circular area of at most ≃166. mm radius (β=1 particle); as a consequence, in the case of the real mirror, at most 3 different adjacent mirror hexagonal elements will be

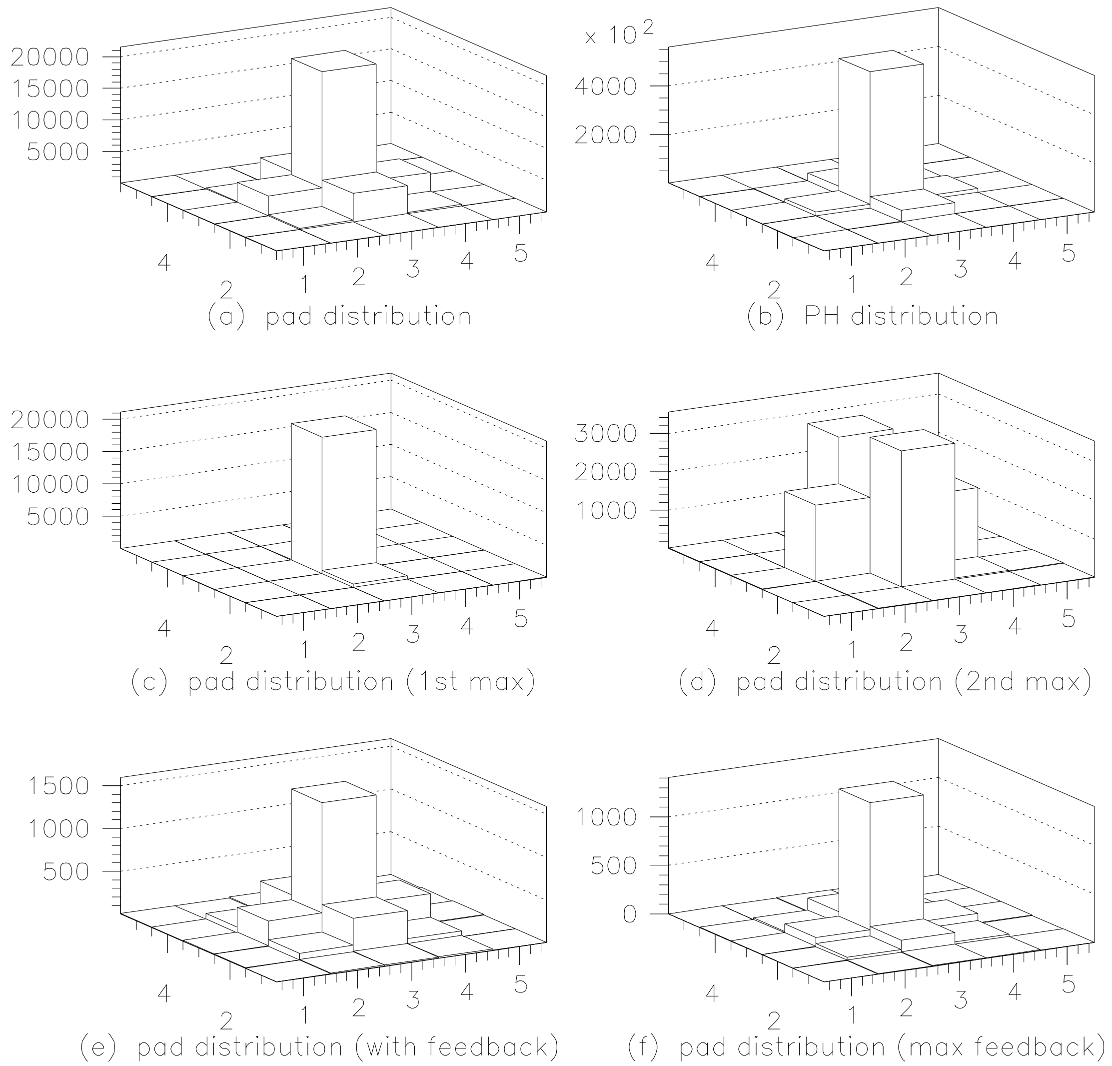

Figure 7: Some typical pad and PH distributions around the pad hit by the incoming photon: (a) active pads; (b) corresponding PH's; (c) pad of the PH maximum; (d) pad of the PH second maximum; (e) pads with a feedback photon converted ($\simeq$ 10%) and (f) pad of the PH maximum of the feedback photon.

involved.
The knowledge of the particle impact point on the mirror will then allow to determine the mirror elements hit by the photons and then adequate corrections to the mirror imperfections.
This procedure has not yet been implemented.

• *Ring* recognition.
The *ring* pattern recognition is then equivalent to a search for a peak in the θ_{clu} projection of the above distribution.
To this purpose, a θ_{clu} bin size of 1. mrad has been chosen, as a function of the expected counts (photons) in the signal peak ($\simeq 30$).
To determine the peak position, counts are integrated within a window 5 bins wide (corresponding to $\sim\pm 3\sigma$ in the *single photon* resolution; see below) and a scan is made over a range in θ_{clu} from 0. up to 70. (or 60.) mrad (the Cerenkov angle for C_4F_{10} radiator and

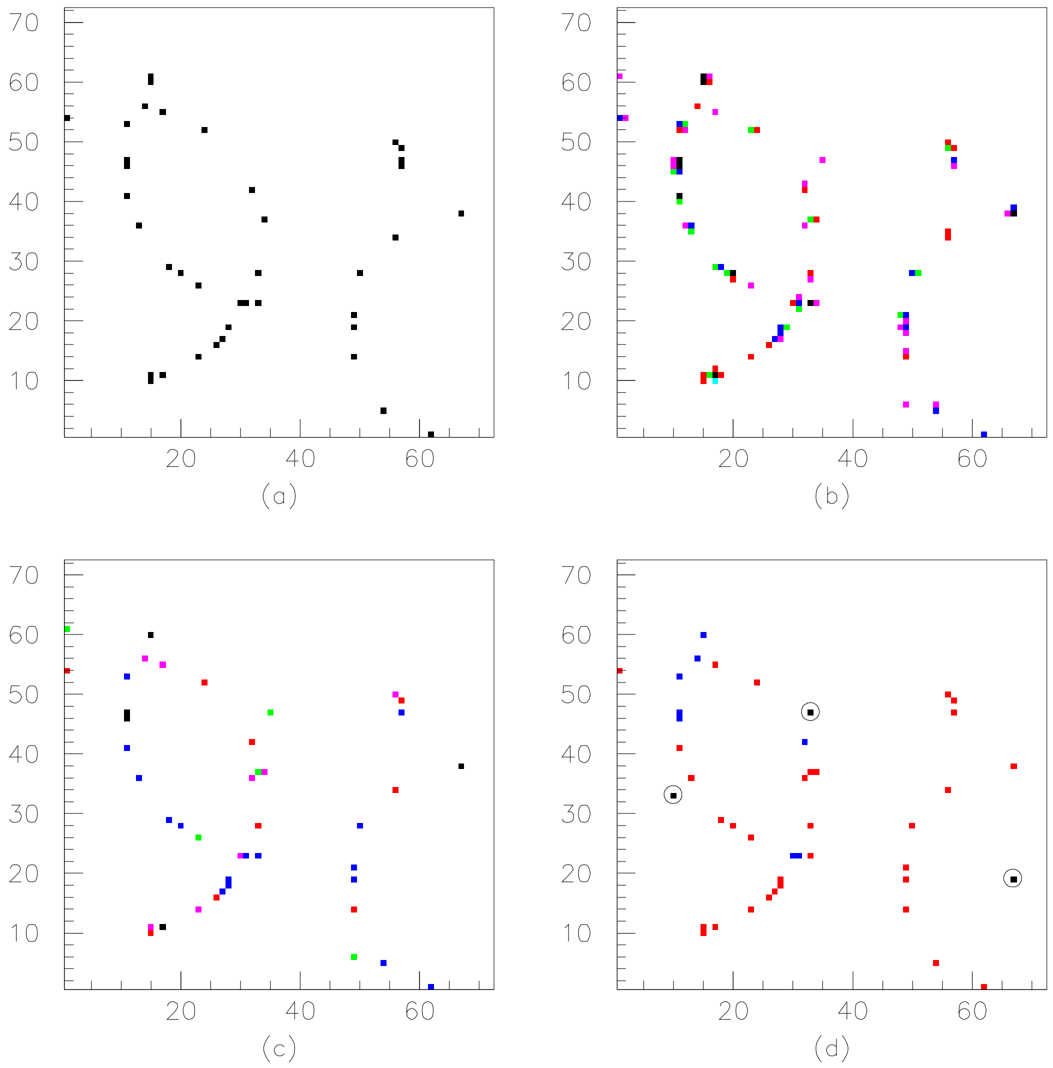

Figure 8: An exemple of a cathode with some *rings* (or parts) in it: in (a) the layout of the pads as hit by the incoming photons; in (b) after pulse generation and electronic noise addition; in (c) the cluster distribution; in (d) the photons belonging to the reconstructed *rings* and the 'virtually reflected' particle impact points (circled).

β=1 particle being 55.3 mrad).
The peak position is assumed to correspond to the maximum in the scan.
The ratio between the integrated counts in the peak window and the background in the peak, from the average outside the peak, is computed as a figure of merit.
In fig.12 this ratio is shown as a function of the particle multiplicity; the increase is quite large.
A first approximation value for θ_{ring} is computed as the average of the θ_{clu} values in the peak; in calculating the average, each θ_{clu} value is taken with equal weight.

In the reconstruction procedure we have to take into account the presence of the quartz entrance window to the detector (5. mm width, 1.458 refractive index), which distorts the incoming photon trajectory for incidence angles different from 90 degrees.
The knowledge, after the first reconstruction step, of the (approximate) reflected photon trajectory, allows the evaluation of the photon incidence angle and then the calculation

of the correction to the photon impact point on the photocathode plane.
A second value for θ_{ring} is then computed.

The standard deviation σ_θ^{photon} of the θ_{clu} - θ_{ring} distribution is assumed as the (inverse) *single photon* resolution ($\simeq$800. μrad) (see fig.13).

In fig.9 the same event as in fig.6; 10 *rings* have been found, among 12, mainly because only 10 have enough photons (i.e. the number of clusters in the peak ≥ 5) to produce acceptable *rings*, as requested in this exemple (in agreement with a by eye recognition).

• *Ring* overlap.
In the case of one particle per event, θ_{ring} is a good measure of θ_C.
For higher particle multiplicities, the probability that *rings* overlap on the detector surface becomes important and, in the ϕ_{clu} vs θ_{clu} plot, the patterns due to photons emitted by the other particles intersect the line along which lie the good ones (see fig.10 (a) to (c)); in the θ_{clu} peak enter unwanted counts, distorting the θ_{ring} value and degrading its resolution.

To limit this effect, a weighted average (a) and a filtering procedure (b) have been tested.
a) For θ_{clu} values belonging to the peak, the corresponding ϕ_{clu} values are uniformly distributed over the 360 degrees; dividing the ϕ range in 120 3° ϕ bins, the expected number of clusters (photons) per bin is 0.25; if a ϕ bin content is larger than 1, it is assumed that patterns due to photons emitted by the other particles intersect there and the θ_{clu} values belonging to the bin enter the θ_{ring} average with weight 0.5.
A further cut in θ_{clu} at $\pm 3\sigma_\theta^{photon}$ around θ_{ring} is applied and a new average calculated.
b) The background filtering procedure acts in the following way :
In the ϕ_{clu} vs θ_{clu} plot relative to particle k, the clusters giving origin to θ_{clu} values within the 'signal' peak are flagged; this is done for all the plots (particles) in which a 'signal' peak has been found.
The search for the 'signal' peak is then restarted, for each particle, in a ϕ_{clu} vs θ_{clu} plot from which have been discarded all the entries flagged as 'signal' for all the particles except the one considered.
See the fig.14 in which the distribution of the difference θ_{clu} - θ_{ring} is shown without and with the background filter, as a function of the particle multiplicity.

5 Results :

In the simulation, both angle resolution and *ring* reconstruction efficiency have been investigated.

• Resolution.
σ_θ^{ring} is evaluated from the distribution of θ_{ring} - θ_{MC}.
In fig.15 the distribution of θ_{ring} - θ_{MC} is shown for events of particle multiplicity of $\simeq$7.7 ('triple' events).
In (a) the integrated distribution; in (b 1-3) as a function of the angle the 'reflected particle' makes with the detector surface (i.e. $\sim$ the average of the angles the photons make):

the larger the angle the greater the departure of the *ring* shape from the circular one and the dispersion of the photon impacts on the detector because of the spherical aberrations of the optics (see the cited COMPASS Internal Note '... Part 2'.). In (c 1-5) as a function of the β of the particle.
It is in fact expected that σ_θ^{ring} is contributed, together with the pad size and the clustering procedure (assumed constant for all particles on the whole detector surface), by the aberrations due to the photon reflection on the spherical mirrors, as taken into account by the angle reconstruction method used, as shown in (b 1-3), and by the ratio between the pixel (pad) dimensions and the *ring* radius (or the β of the particle), as shown in (c 1-5).

• Efficiency.
The *ring* reconstruction efficiency is evaluated counting the ratio between 'successes' and incoming particles, a 'success' being a reconstructed *ring* with $|\theta_{ring}$ - $\theta_{MC}|$ less than $\Delta\theta_{cut} \simeq 3\ \sigma_\theta^{ring}$ (700.-800.μrad).
$\Delta\theta_{cut}$ can be parametrized as a function of the β of the particles and their multiplicities.

• Procedure tuning.
The results of a first step in the tuning of the procedure are summarized in table 1 :
In the first column, the lower limit (or cut) of the momentum distribution used;
<n> is the average particle multiplicity (in parenthesis, the number of events combined together);
σ_θ^{ring}, as from a gaussian fit to the θ_{ring} - θ_{MC} distributions, normalized to 34 photons per *ring*, for comparison with the figures of the proposal;
$<N_r>$ is the average number of photons found per *ring*;
ϵ, the *ring* reconstruction efficiency as defined above.
In the last column are specified the different conditions in which the reconstruction has been done :
[P] : Pixel (Pad) only,
[SA]+[P] : mirror Spherical Aberrations and Pixel only,
[all] : [SA] + [P] + pad induction and pulse height thresholding + feedback photons and electronic noise + pad clustering;
[all]-[Clu] : no pad Clustering,
$^{(1)}$: PH fixed in input pads.
The scan for peak in θ_{clu} is up to 70 mrad.
For high momentum (or β) particles and mirror spherical aberrations and pixel only, the agreement between θ_{ring} and the value of the proposal (first and last row) is quite good. Using all the active pads without clustering, seems not to degrade too much the resolution, at least for high momentum particles; on the other hand, the increase of the particle multiplicity (*ring* overlap) results in an appreciable increase of σ_θ^{ring}.

• Weighted average and background filter tuning.
In table 2 the tuning of the procedures of the weighted average [ϕ] and of the bakground filter [f] respectively are shown.
<n>, σ_θ^{ring} and ϵ as for table 1;
$<N_t>$ is the average number of incoming photons over threshold and $<N_r>$ the average number of reconstructed photons per *ring* (particle).
$^{(1)}$ means that no pad induction and no feedback photons are simulated at the signal

$p_p \geq$ GeV/c	<n>	$\sigma^{ring}_{\theta\ 34*}$ μrad	<N_r >	ϵ %	notes
20.	1	132.*	20.6	99.8	[SA]+[P]
20.	1	138.*	16.8	99.8	[all]
20.	1	(145.*)	(32.3)	99.6	[all]-[Clu]
20.	2.4(2)	170.*	20.6	99.2	[all]
20.	2.4(2)	(172.*)	(35.7)	99.2	[all]-[Clu]
~2.	5.6(2)	185.*	17.1	94.6	[all]
20.	3.6(3)	173.*	19.3	97.8	[all]
~2.	7.7(3)	210.*	18.3	92.8	[all]
~2.	12.8(5)	235.*	19.5	81.	[all]
60.	1	120.	34		Prop.[P]
60.	1	132.	34		[SA]+[P]

Table 1: σ^{ring}_{θ} is the standard deviation of the reconstructed Cerenkov emission angle θ, normalized to 34 photons per *ring*, and ϵ the reconstruction efficiency; <n> the average number of particles per event (event$\times$k) and <N_r > the average number of reconstructed photons per *ring* (particle). See the text for the other specifications.

generation level, $^{(2)}$ no electronic noise on the detector pads;
$^{[2\sigma]}$ and $^{[3\sigma]}$ is for a 2 or 3 σ^{photon}_{θ} cut around the 'signal' peak in bakground filter;
[Clu] means no pad clustering, with PH of pads fixed.
The scan for peak in θ_{clu} is up to 70 mrad.
Note that in this table σ^{ring}_{θ} corresponds to N_r photons per *ring*.
The first and the second part of the table are for a better understanding of the detector behaviour.
Clustering and 2 σ^{photon}_{θ} cut seems to be the best conditions.

• Comparison of the weighted average and the bakground filter.
In table 3 the comparison of the results from the weighted average [ϕ] and the bakground filter [f] are shown;
<n>, <N_r >, σ^{ring}_{θ} and ϵ as for table 1 and 2; N_p is the average number of counts in the peak.
The scan for peak in θ_{clu} is up to 60 mrad.
$\sigma^{ring}_{\theta c}$ is σ^{ring}_{θ} as calculated from σ^{photon}_{θ} divided by $\sqrt{N_r - 1}$; the agreement with σ^{ring}_{θ} is better when the bakground filter is used; also better for the bakground filter are the resolution σ^{ring}_{θ} and the efficiency ϵ, for all particle multiplicities.
The behaviour of $\sigma^{ring}_{\theta c}$ and <N_r > as a function of the photon density on the detector surface (particle multiplicity) indicates some undercorrection for *ring* overlap in the case of weighted average and some overcorrection for the bakground filter; further tuning is needed.

• The evolution of the photon counts through the procedure is summarized in fig.16 (distributions at 7.7 particles per event) and in table 4 (average values, as a function of the particle multiplicity).
In fig.16 (a) there is the distribution of the number of converted photons per particle,

<n>	<N_t >	<N_r >		σ_θ		ϵ		notes
		[ϕ]	[f]	[ϕ]	[f]	[ϕ]	[f]	
7.7	18.4	20.0	16.2	241	219	96.9	99.1	(1)(2)[3σ]
7.7	18.4	20.0	17.1	241	218	96.9	99.1	(1)(2)[2σ]
7.7	18.4	20.0	18.6	241	227	96.9	98.4	(1)(2)[1σ]
7.7	16.3	17.5	15.2	238	210	96.6	99.0	(2)[2σ]
7.7	16.3	17.5	14.2	238	211	96.6	98.9	(2)[3σ]
7.7	16.3	18.0	15.6	242	215	95.6	98.1	[2σ]
7.7	16.3	18.0	14.8	242	215	95.6	97.8	[3σ]
7.7	16.3	23.5	25.5	265	240	95.3	98.1	[Clu]$^{[2\sigma]}$
7.7	16.3	23.5	23.9	265	238	95.3	98.4	[Clu]$^{[3\sigma]}$
7.7	16.3	23.5	22.9	265	242	95.3	98.2	[Clu]$^{[4\sigma]}$

Table 2: σ_θ ($= \sigma_\theta^{ring}$) and the efficiency ϵ in the reconstruction of the Cerenkov emission angle θ; the effects of the weighted average [ϕ] and of the background filter [f] are shown, in different conditions. <n> is the average number of particles per event and <N_r > the average number of reconstructed photons per *ring* (particle). The cluster weight is fixed in the average of the θ values.

in (b) of the number of pads hit by one or more photons, in (c) of the useful photons (above the threshold and in the sensitive area of the detector), in (d) of the number of clusters found per particle, in (e) of the cluster number in the *ring* peak and in (f) after the filtering procedure.
In table 4 the corresponding average values <N_i >, <N_h >, <N_t >, <N_c >, <N_p > and <N_f >.
The first three columns should be multiplicity independent (as they are); the fourth one (clusters found) is very little dependent, denoting a good performance of the clustering code; the cluster number in the *ring* peak (fifth column) depends on the *ring* overlap, but the cluster number in the *ring* after filtering (last column) shows again a reduced dependence on the particle multiplicity; note that this behaviour is better than that of <N_r > in table 3 because of a further tuning of the filtering procedure ([1σ] cut used).

• Particle identification.
As stated in the introduction, this is not a particle identification procedure.
However, to give a visual appreciation of the meaning of the angle resolution and a check of the general consistency, particle masses have been assigned looking for the value of θ_{ring} reconstructed closest to the θ values calculated from the masses of the π, K and p respectively at fixed momenta; in table 5 the assignements are reported, as a function of the particle momentum together with the fraction of wrong identifications.
The relevant feature is the π-K separation, whereas the π mass cannot be easily separated from lower masses.
Moreover, particle masses have been calculated at fixed momenta from the measured θ_{ring} and their distributions can be compared in fig.17.
In this simulation an equal number of masses of fixed momentum, with uniform illumination of the mirror surface, has been generated; the figures obtained are indicative only.

<n>	N_p	σ_θ^{phot} $[\phi]$	σ_θ^{ring}	$<N_r>$	$\sigma_{\theta c}^{ring}$	ϵ	σ_θ^{phot} $[f]$	σ_θ^{ring}	$<N_r>$	$\sigma_{\theta c}^{ring}$	ϵ
1.	17.2	767	209	16.4	195.4	98.9	765	208	16.9	192.4	98.9
2.6	17.7	769	216	16.7	194.1	98.3	765	208	16.6	193.7	98.8
5.2	18.7	782	231	17.2	194.3	97.1	767	212	16.1	197.4	98.7
7.7	19.6	791	248	17.8	193.0	96.2	768	222	15.6	201.0	98.4
10.2	20.5	798	260	18.3	191.9	94.9	768	223	15.1	204.5	98.1
12.8	21.3	808	280	19.0	190.4	93.7	766	236	14.6	207.7	97.4
1.[20]	19.2	737	190	17.8	179.8	99.8	733	188	18.8	173.7	99.8

Table 3: Comparison of the weighted average $[\phi]$ and the bakground filter $[f]$, as a function of the photon density on the detector surface; <n>, $<N_r>$, σ_θ^{ring} and ϵ as for table 2; N_p is the average number of counts in the peak; $\sigma_{\theta c}^{ring}$ is calculated from σ_θ^{photon} dividing by $\sqrt{N_r - 1}$. The behaviour of $\sigma_{\theta c}^{ring}$ and $<N_r>$ indicates some undercorrection for *ring* overlap in the case of weighted average and some overcorrection for the bakground filter; [20] means momentum larger than 20. GeV/c.

<n>	$<N_i>$	$<N_h>$	$<N_t>$	$<N_c>$	$<N_p>$	$<N_f>$
2.6	20.0	18.6	16.3	16.7	17.3	16.7
7.7	20.0	18.5	16.3	16.5	18.7	16.7
12.8	20.0	18.5	16.3	16.3	20.0	16.5

Table 4: The average values of photon or cluster per particle at different steps of the recontruction procedure, as a function of the particle multiplicity. The good performance of the clustering recipe (column four) and of the filtering procedure (column six) is outlined. See the test for more details.

p_p	m_π	σ_m	π		m_K	σ_m	K		m_p	σ_m	p	
			π	K			K	π			p	K
10.	.139	.008	97.0	0.	.493	.001	100.	0.	.940	.009	100.	0.
20.	.137	.029	67.6	0.	.493	.007	100.	0.	.939	.005	100.	0.
30.	.149	.045	55.9	0.	.492	.018	100.	0.	.937	.009	100.	0.
40.	.175	.068	54.3	0.1	.491	.032	99.9	0.1	.938	.017	100.	0.
50.	.198	.083	48.5	1.8	.485	.056	97.6	2.4	.936	.030	100.	0.
60.	.236	.105	44.2	7.3	.481	.083	91.	8.7	.935	.040	100.	0.

Table 5: Reconstructed mass values and σ_m for particles of fixed momentum from the distributions of fig.17; masses are calculated from the reconstructed Cerenkov emission angle θ_{ring}. In the other columns the correct or wrong mass assignements obtained finding the closest match of θ_{ring} to the angle values calculated from the π, K or p mass. Momenta are in GeV/c and m and σ_m in GeV/c^2.

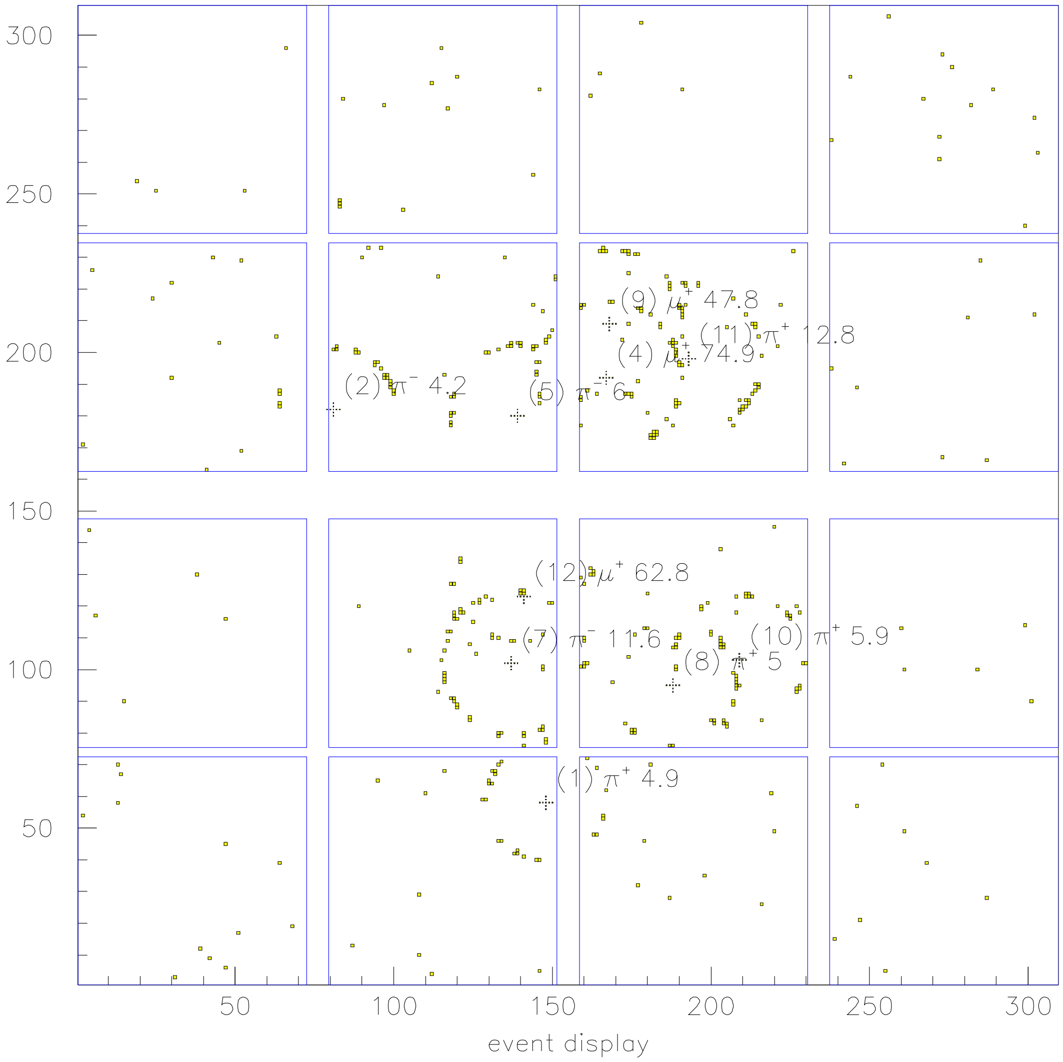

Figure 9: Display of the same event as in fig.6 after reconstruction: 10 *rings* have been found; type and momenta (GeV/c) of the particles (as from input data) are indicated. The particles in the event are 12, but only 10 have enough photons (i.e. clusters in the peak ≥ 5) to produce acceptable *rings*, as requested in this exemple and in agreement with a by eye recognition; the crosses correspond to the inpact points on the detector of the particles 'virtually reflected' from the mirror for which the *rings* have been recognized.

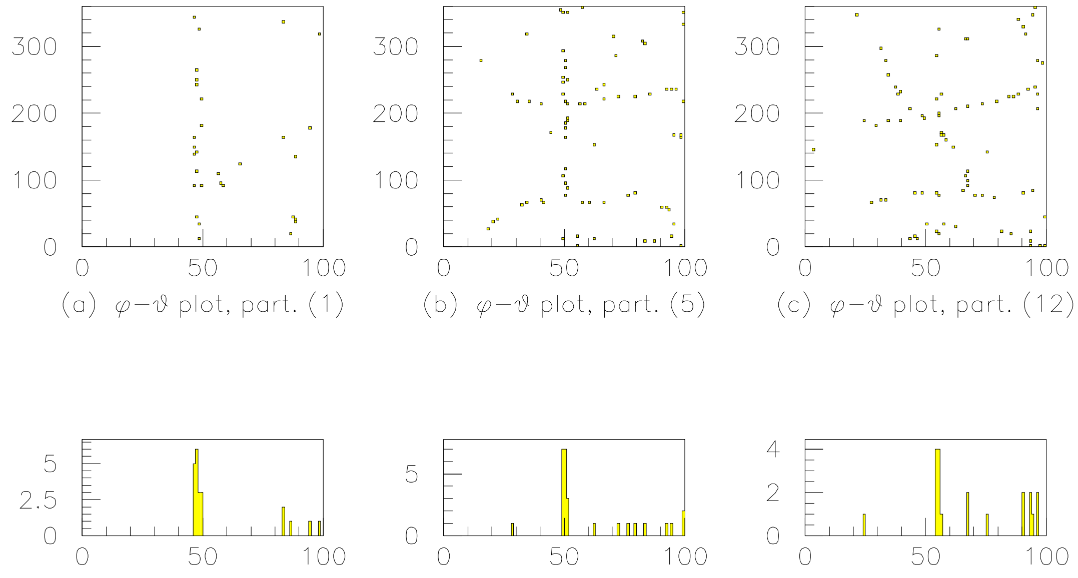

(a) $\varphi-\vartheta$ plot, part. (1) (b) $\varphi-\vartheta$ plot, part. (5) (c) $\varphi-\vartheta$ plot, part. (12)

(d) ϑ proj., part. (1) (e) ϑ proj., part. (5) (f) ϑ proj., part. (12)

Figure 10: Plot ϕ_{clu} vs θ_{clu} and relative projection on θ-axis for particle (1), (5) and (12) of the event displayed.

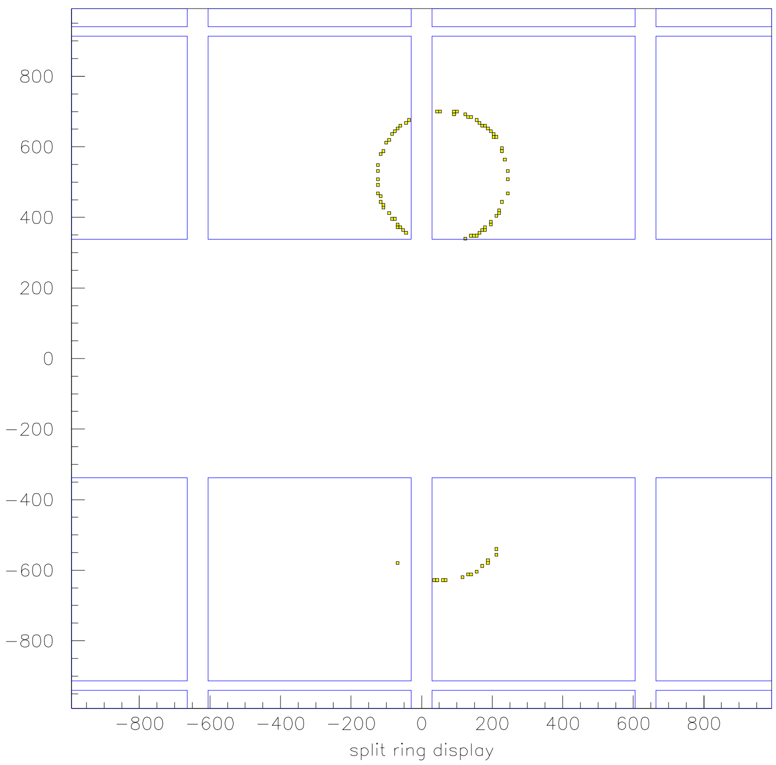

Figure 11: Exemple of a *ring* generated by a particle illuminating both the (upper and lower) mirrors and split between the two detectors.

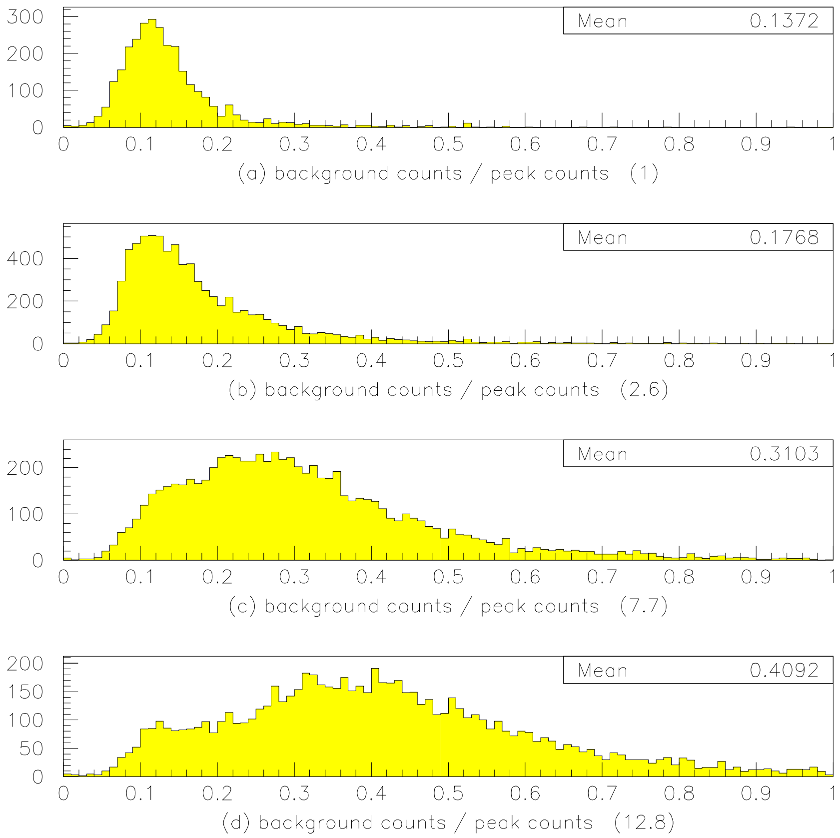

Figure 12: The ratio of the integrated counts in the peak window to the background in the peak, computed from the count average outside the peak, for different particle multiplicities (in parenthesis the number of particles per event).

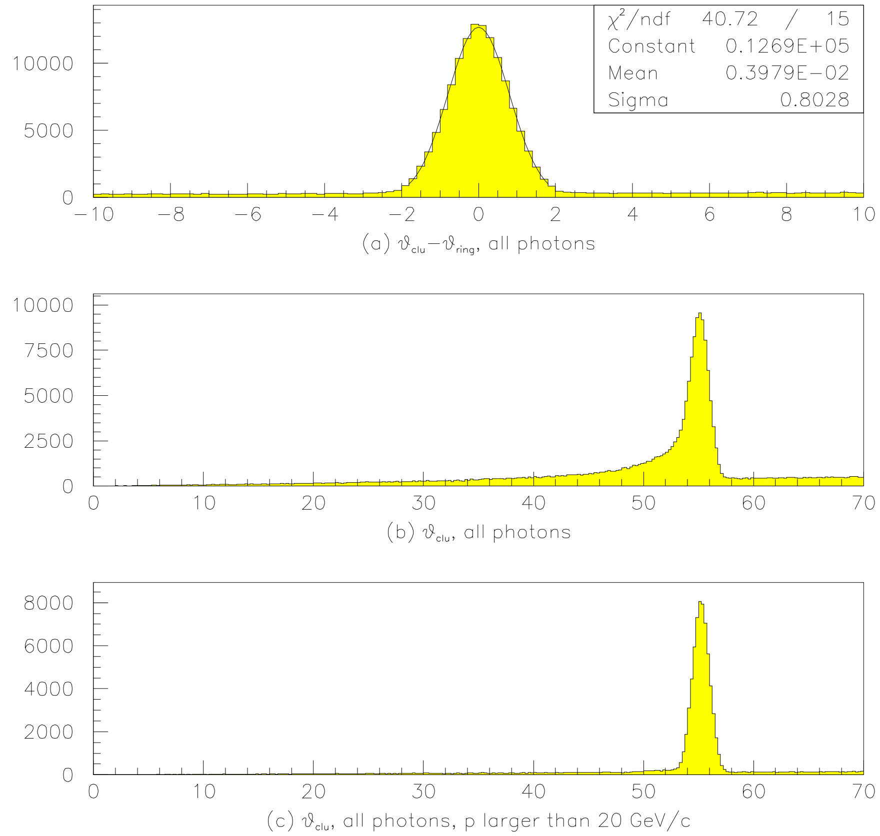

Figure 13: The distribution of θ_{clu} - θ_{ring} is shown (a) for all the photons for each particle, for 'triple' events ($\simeq 7.7$ particles per event); the width of the distribution gives an estimate of σ_{θ}^{photon} (*single photon* resolution). In (b) the θ_{clu} distribution for all the particles is shown; the shape of the background corresponds, to a first approximation, to an uniform distribution over the detector surface; same particle density as in (a). In (c) as in (b), but for particles of momentum $\geq$20. GeV/c ($\beta\simeq$1.). Units are mrad.

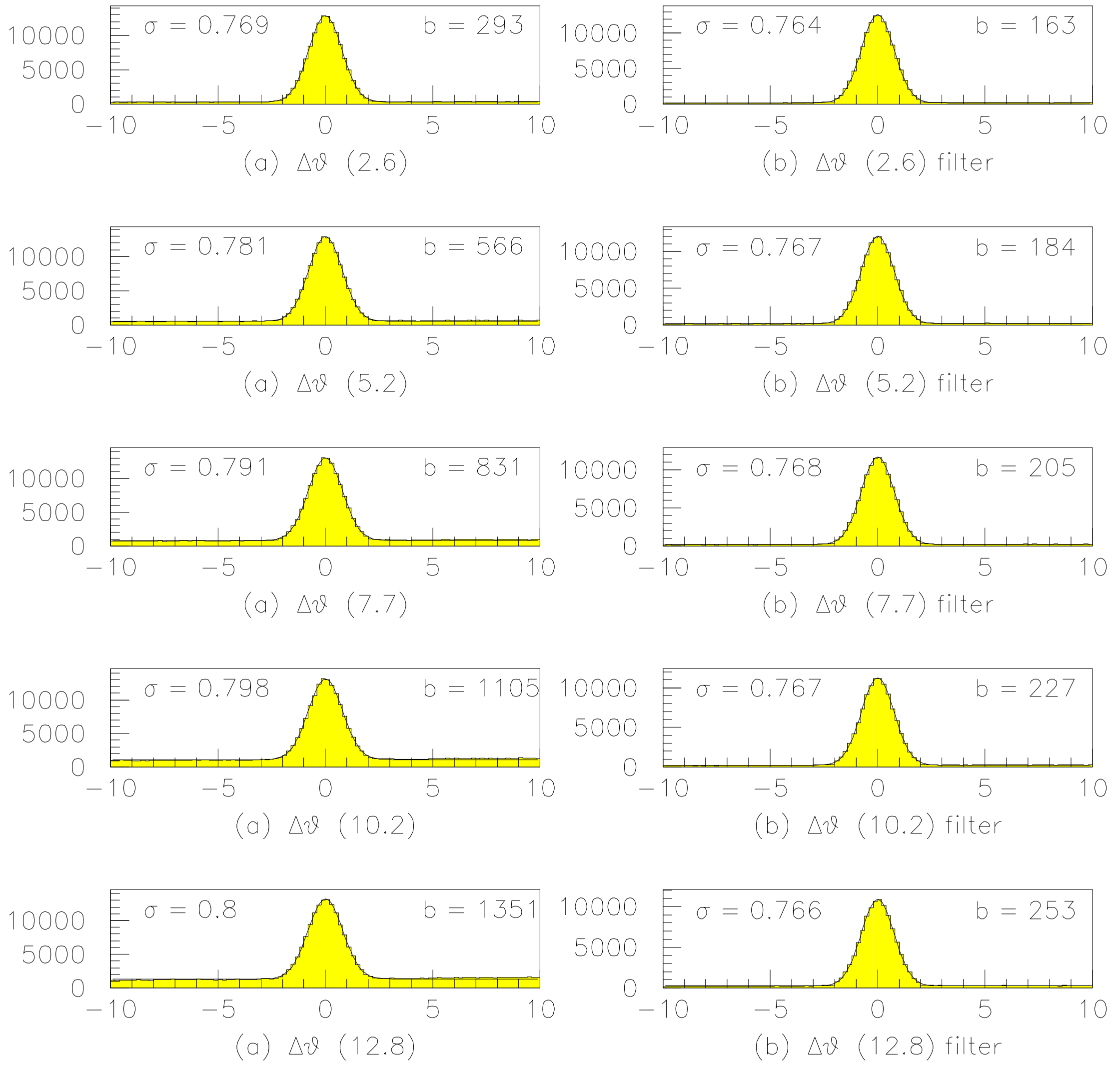

Figure 14: The figure shows the distribution of $\Delta\theta$ ($= \theta_{clu}$ - θ_{ring}), without (column (a)) and with (column (b)) the background filter, as a function of particle multiplicity (in parenthesis); note how σ becomes more constant and the background b largely reduced.

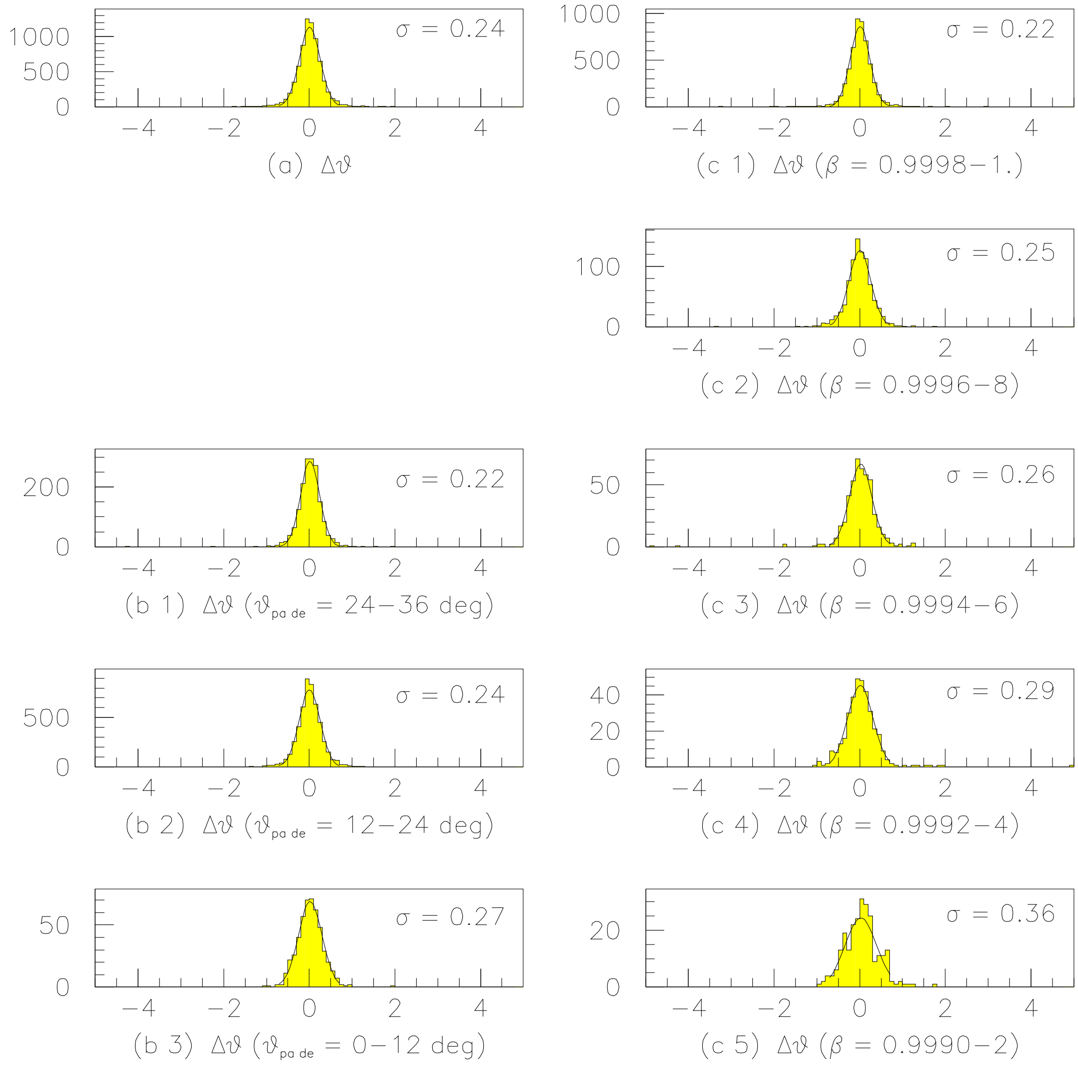

Figure 15: The figure shows the distribution of $\Delta\theta$ ($= \theta_{ring}$ - θ_{MC}), from which the (inverse) resolution σ_θ^{ring} is computed; units are mrad; 'triple' LEPTO events ($\simeq$7.7 particles per event). In (a) for all the particles. In (b 1-3) σ_θ^{ring} as a function of the angle the 'reflected particle' makes with the detector surface. In (c 1-5) σ_θ^{ring} as a function of the β of the particle. The distributions are without the background filter. Note that σ_θ^{ring} is equivalent to σ_θ^{photon} divided by the square root of the number of photons in the *ring* (17.8 in average in this simulation; to be compared with the reference figure of 34).

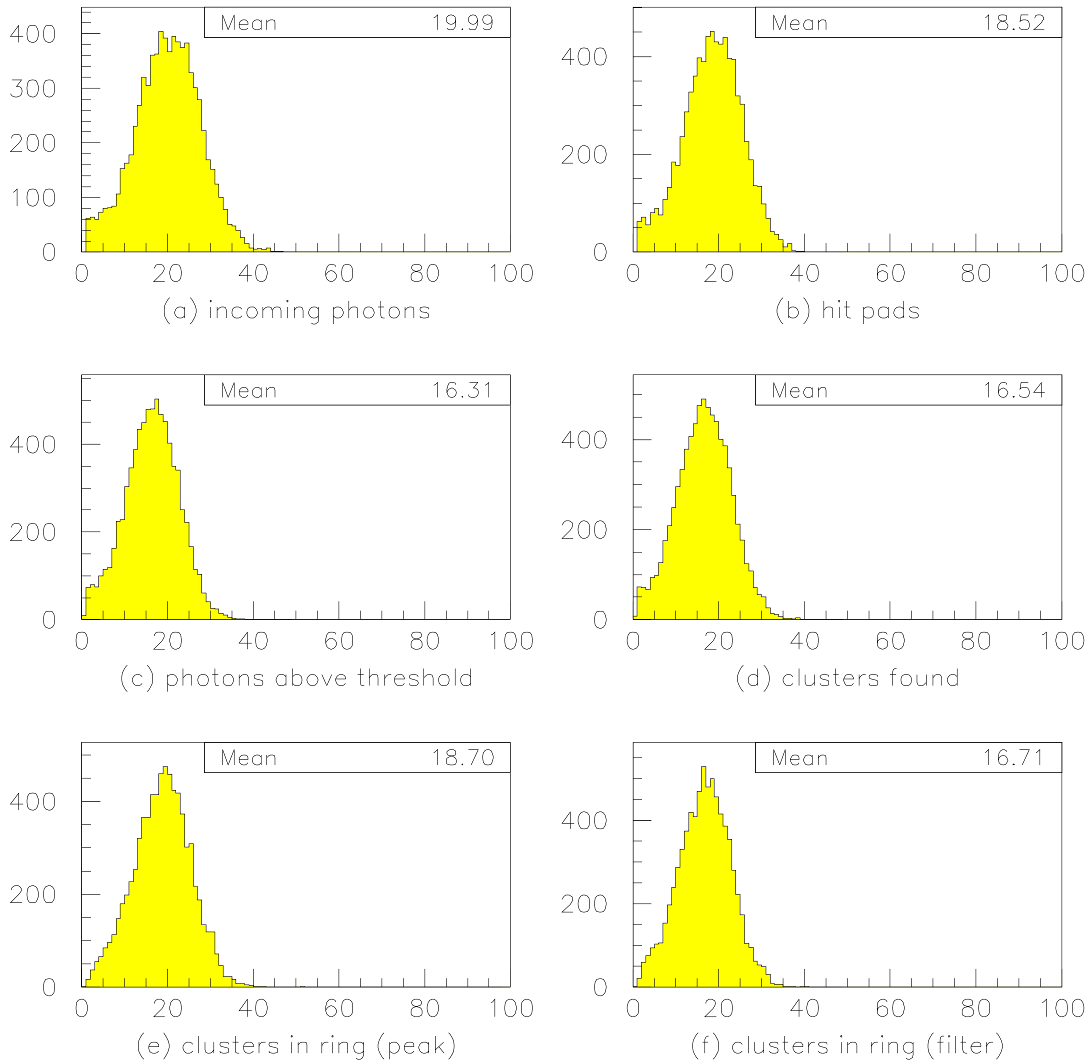

Figure 16: The distributions of the number of counts (photons or clusters) at different steps of the reconstruction procedure, for a particle multiplicity of 7.7 particles per event. See the text for more details.

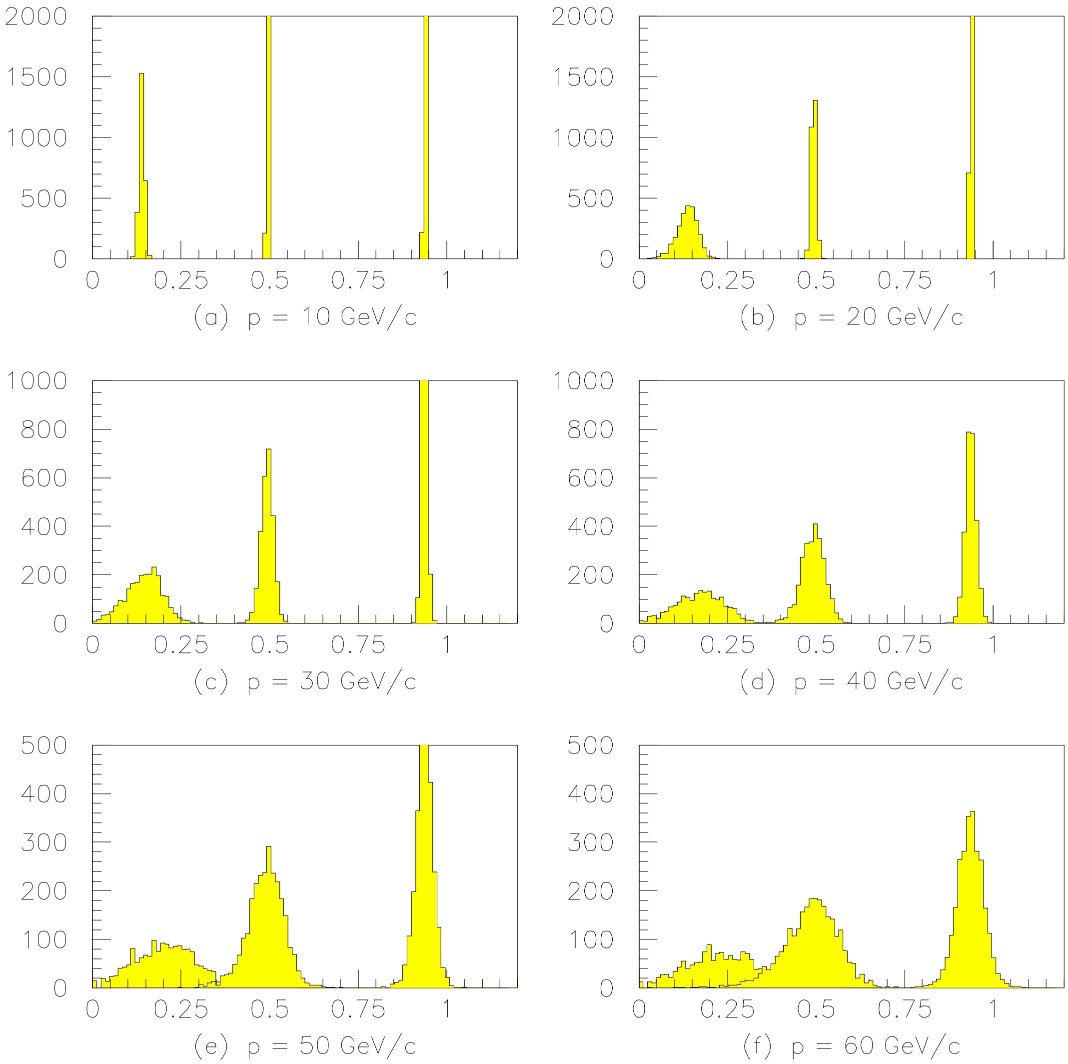

Figure 17: The masses of π, K and p, as calculated from the reconstructed Cerenkov emission angle θ_{ring}, at the fixed momentum values indicated.